Correspondence to:
W. S. Moore,
moore@geol.sc.edu

Enriched Regions of [228]Ra Along the U.S. GEOTRACES Pacific Meridional Transect (GP15)

Willard S. Moore[1] , **Matthew A. Charette[2]** , **Paul B. Henderson[2]**, **Douglas E. Hammond[3]**, **Nathaniel Kemnitz[3]**, **Emilie Le Roy[4]** , **Eun Young Kwon[5]** , and **Mikael Hult[6]**

[1]School of Earth, Ocean & Environment, University of South Carolina, Columbia, SC, USA, [2]Woods Hole Oceanographic Institution, Woods Hole, MA, USA, [3]Department of Earth Sciences, University of Southern California, Los Angeles, CA, USA, [4]UMR 6539 LEMAR, CNRS, IRD, Ifremer, University of Brest, Plouzane, France, [5]Center for Climate Physics, Institute for Basic Science, Busan, South Korea, [6]European Commission, Joint Research Centre (JRC), Geel, Belgium

Abstract The half-life of [228]Ra (5.7 years) aligns well with near-surface and near-bottom ocean mixing timescales. Because [228]Ra is sourced from sediments, regions of enhanced activity represent water that has recently interacted with sediments on the continental margin or seabed. The GP15 meridional transect from Alaska to Tahiti along 152°W encountered several regions in the upper ocean where [228]Ra was enriched. These enrichments follow surface and subsurface ocean current patterns and pair with earlier measurements of [228]Ra and transient radionuclides to reveal the origins of these enriched regions. An enriched region at Alaska margin stations 1–3 was sourced locally but did not extend to the Alaskan trench at station 4. A large shallow region between 47° and 32°N. was sourced from the west by the North Pacific Current; another shallow enriched region between 11° and 5° N was also sourced from the west by the North Equatorial Countercurrent. Subsurface enrichments (100–400 m) between 18 and 47°N were associated with Central Mode Water and North Pacific Intermediate Water. The [228]Ra activities in the upper Pacific were six times lower than activities in the Atlantic. In deep waters the primary enrichment was 27°–47°N. Two stations (32° and 37°N) were especially enriched, having near-bottom inventories several times greater than other stations. With these two exceptions the remaining Pacific stations exhibited averaged inventories lower than those in the Atlantic. There was one region of enriched [223]Ra (half-life = 11 days) above the Puna Ridge near Hawaii.

Plain Language Summary The international GEOTRACES program aims to identify processes and quantify fluxes that control the distribution of trace elements and isotopes (TEIs) in the ocean. Some TEIs are important micronutrients, which may control biological productivity. Others may become concentrated as they pass up the food web and reach potentially harmful levels in some seafood. But measurements of these TEIs are not adequate to determine controlling processes or quantify their fluxes in the marine environment. Radionuclide tracers provide a means to link TEI measurements with fluxes and processes. Here we employ measurements of [228]Radium (half-life = 5.75 years) to trace water movements and current speeds in the upper Pacific and to determine regions near the seabed where sediment-water interactions are most intense. The upper ocean measurements confirmed a broad circulation pattern that brought water from the Asian margin to the northeast Pacific at speeds of 2–8 cm/sec, in agreement with other estimates of these current speeds. Near the seabed we discovered a region of enhanced [228]Ra activity indicating intense sediment-water interactions. Such regions may control the release of TEIs from the seabed to the water column. We anticipate others will utilize these data to elucidate aspects of other TEI distributions.

1. Introduction

The goal of the International GEOTRACES Project is to "Identify processes and quantify fluxes that control the distribution of trace elements and isotopes (TEIs) in the ocean and to establish the sensitivity of these distributions to changing environmental conditions" (Anderson, 2020; SCOR, 2007). The naturally occurring radium isotopes ([226]Ra, $t_{1/2}$ = 1,600 y; [228]Ra, $t_{1/2}$ = 5.75 y; [223]Ra, $t_{1/2}$ = 11.4 d; [224]Ra, $t_{1/2}$ = 3.66 d provide a set of isotopes called the "Radium Quartet" that enables the identification of processes and quantification of fluxes that control the distributions of other TEIs.

Nathaniel Kemnitz, Emilie Le Roy, Eun Young Kwon, Mikael Hult
Methodology: Willard S. Moore, Matthew A. Charette, Paul B. Henderson, Douglas E. Hammond, Nathaniel Kemnitz, Emilie Le Roy, Mikael Hult
Project administration: Matthew A. Charette
Resources: Willard S. Moore, Matthew A. Charette, Paul B. Henderson, Douglas E. Hammond, Nathaniel Kemnitz, Mikael Hult
Software: Paul B. Henderson, Douglas E. Hammond, Nathaniel Kemnitz, Eun Young Kwon
Supervision: Matthew A. Charette
Validation: Willard S. Moore, Matthew A. Charette, Paul B. Henderson, Douglas E. Hammond, Nathaniel Kemnitz, Mikael Hult
Visualization: Eun Young Kwon
Writing – original draft: Willard S. Moore, Matthew A. Charette
Writing – review & editing: Willard S. Moore, Matthew A. Charette, Paul B. Henderson, Douglas E. Hammond, Nathaniel Kemnitz, Emilie Le Roy, Eun Young Kwon, Mikael Hult

1.1. Early ^{226}Ra and ^{228}Ra Studies

Early ocean radium measurements were focused on the use of ^{226}Ra to measure vertical mixing in the deep ocean (Koczy et al., 1957). The GEOSECS Project (1972–1979) compiled detailed data on the distribution of ^{226}Ra in the world ocean while attempting to use its distribution to measure mixing rates (Chung, 1980; Chung & Craig, 1980; Ku & Luo, 1994). Efforts to calculate mixing rates based on ^{226}Ra decay were largely unsuccessful because the measurements revealed that scavenging of ^{226}Ra in the upper water column was considerably more important than radioactive decay in controlling its distribution (Broecker & Peng, 1982). An intriguing result of the Pacific GEOSECS measurements was the identification of a high-source region of ^{226}Ra in the deep northeast Pacific at ~30°N, 130–160°W.

Although ^{228}Ra measurements were included in the GEOSECS Project, the initial data were sparse due to processing and recovery issues (Li et al., 1980). The discovery that radium could be quantitively scavenged onto acrylic fibers coated with manganese dioxide (Moore & Reid, 1973) provided a means of rapidly processing large volumes of seawater for ^{228}Ra measurements and led to detailed vertical profiles near the seabed (Moore, 1976; Moore & Santschi, 1986; Sarmiento et al., 1982) during the later GEOSECS years.

1.2. Studies of ^{228}Ra Since 2000

Since the turn of the 21st century there has been a renaissance of the use of radium isotopic tracers in marine processes studies (Charette & Scholten, 2008); many of these studies have been pioneered in conjunction with GEOTRACES. Measurements of the distribution of a stable trace metal alone, for example, Fe, Mn or Co, no matter how accurate, are not sufficient for determining controlling processes or quantifying trace element and isotope (TEI) fluxes—a central goal of the GEOTRACES program. For example, Charette et al. (2016) demonstrated that by combining model-derived shelf ^{228}Ra fluxes with TEI/^{228}Ra ratios, they were able to quantify ocean TEI fluxes from the western North Atlantic margin. Sanial et al. (2018) used a similar approach to quantify dissolved manganese, iron, and cobalt fluxes from the Peruvian margin that extended over 1,800 km into the central Pacific. The discovery of high ^{228}Ra activities in the Trans Polar Drift (Kipp, Charette, et al., 2018; Rutgers van der Loeff et al., 1995) led to the realization that this current was responsible for supplying TEIs as far as the North Pole (Charette et al., 2020). Kipp, Sanial, et al. (2018) derived ages of hydrothermal plumes based on ^{228}Ra and used these ages to calculate a residence time of hydrothermal iron in the range of 9–20 years, again illustrating the usefulness of this isotope to TEI studies.

Here we present an overview of Ra isotope (primarily ^{228}Ra) distributions during the U.S. GEOTRACES Pacific Meridional Transect (GP15). We focus on regions displaying relatively high ^{228}Ra activities including (a) the Alaska margin, (b) the upper water column between 27° and 52°N, 152°W, (c) the upper water column near the equator, 5°–11°N, 152°W, (d) deep waters between 27° and 47° N, 152°W, and (e) water above the Puna Ridge near Hawaii where ^{223}Ra was highly enriched. We encourage investigators of other TEIs to consider the Ra distributions in their interpretations.

2. Methods

All samples were collected on the R/V Roger Revelle during the U.S. GEOTRACES Pacific Meridional Transect (GEOTRACES GP15) from the Alaska shelf to Tahiti, primarily along 152° W. longitude (Figure 1).

2.1. Sample Collection Procedure

2.1.1. Preparation of Cartridge Adsorbers

The primary step in sample collection was the adsorption of radium onto a series of filter cartridges that had been impregnated with MnO_2 (Mn-cartridges). The Mn-cartridges were attached to in situ pumps that passed water through filters, then through the Mn-cartridges. One set of Mn-cartridges, which were used as the initial or "A" cartridges were prepared at WHOI using the procedure of Henderson et al. (2013). A second set of Mn-cartridges, which were used as the secondary adsorbers, or "B" cartridges were prepared at U. Southern California using the procedure of Kemnitz (2023).
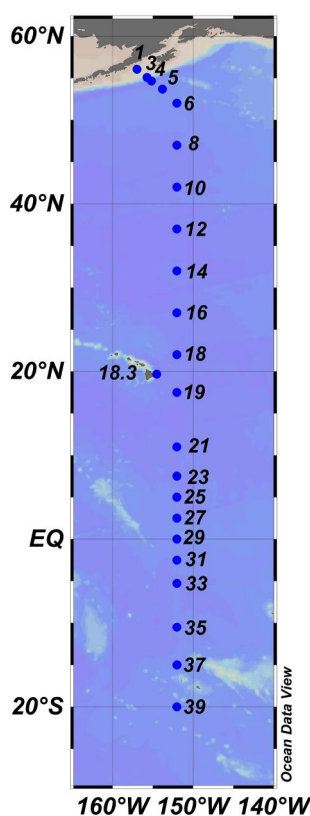
Figure 1. Map of GP15 transect, indicating deep stations sampled for[228]Ra.

2.1.2. Shipboard Procedures

The methods used for measuring the four radium isotopes are described in detail by Henderson et al. (2013). These methods were modified for the U.S. GEOTRACES Eastern Pacific Zonal Transect (GP16) (Sanial et al., 2018) and additional modifications were made for the GP15 measurements. The procedure enables the collection of large volume (>1,000 L) water column samples for ^{228}Ra, ^{224}Ra, ^{223}Ra, ^{228}Th and ^{227}Ac and small volume (15–25 L) samples for ^{226}Ra measurements. In addition to the water column samples, large volume surface samples were collected by pumping from a depth of 2 m through a single Mn-cartridge accompanied by a 15–25-L sample that was passed through a 15 g Mn-fiber column to retain ^{226}Ra (see SI-1 for analytical method).

Figure 2 illustrates the water column sample collection, processing, and analytical procedures for Ra isotopes employed on GP15. The large volume collection system was a modified McLane in situ pump with dual filter heads to collect particulates. The flow was then combined into a single stream and passed through two MnO_2 adsorber cartridge holders connected in series (A and B cartridges) for scavenging dissolved (<1 μm) radium, thorium, and actinium isotopes from seawater (Charette et al., 2015). The pump collection period was 4 hr at a setting of 8 L/min; depending on particle loading, sample sizes generally ranged from 1,300 to 1,700 L. At these flow rates, the scavenging efficiency of the Mn-cartridge is <100%; therefore, small volume samples for ^{226}Ra (15–25 L) were collected from a Niskin bottle mounted above the pump (for samples collected >1,000 m depth) or on a CTD rosette (for shallower samples) and ^{226}Ra was quantitatively extracted onto 15 g Mn-fiber at a flow rate <0.5 L/min to determine ^{228}Ra recovery efficiency.

2.2. Analysis of ^{223}Ra, ^{224}Ra, ^{228}Th, ^{227}Ac, and ^{226}Ra by Delayed Coincidence Counting (RaDeCC)

Mn-cartridge samples were rinsed with deionized water, which had been passed through a Mn-cartridge, and dried with filtered compressed air to remove excess moisture in preparation for analysis via delayed coincidence counting (RaDeCC; Moore and Arnold, 1969). The target water content of the cartridges for analysis of samples and standards was 2:1 (wet/dry weight). Each sample was analyzed three times: after ~36 hr, 4 weeks, and 2 months post collection. The second and third analyses were used to determine the supported ^{224}Ra (from ^{228}Th) and ^{223}Ra (from ^{227}Ac), respectively. The first and second counting cycles consisted of up to two 180 min periods separated by a ~10-min flushing of the counting cells to minimize buildup of ^{222}Rn and its progenies, which can adversely affect the chance coincidence calculations for the ^{224}Ra daughter ^{220}Rn (Moore, 2008). The third cycle was for ~20 hr with no flushing of the counting cell, since the chance coincidence corrections for ^{219}Rn are largely unaffected by ^{222}Rn buildup in the system. The third cycle RaDeCC counting data were also used to determine the activity of ^{226}Ra on the cartridges, which can be quantified from the slope of the total counts per minute versus time due to ingrowth of ^{222}Rn and its daughters (Diego-Feliu et al., 2020; Geibert et al., 2013).

The RaDeCC counters were calibrated with Mn-cartridges doped with ^{226}Ra, ^{232}Th, and ^{227}Ac standards (with daughters in secular equilibrium). Briefly, the Mn-cartridges were placed in 1-L plastic bags along with 300 mL of Ra-free seawater. The standard solutions were added to the bags and placed on a shaker table for 72 hr. The Mn-cartridges were air dried for 24 hr after which they were prepared for counting in the same manner as described above. The residual solution was passed through a MnO_2 acrylic fiber and analyzed for ^{226}Ra (via ^{222}Rn emanation) and RaDeCC; these measurements indicated that >99% of the added tracers had adsorbed to the Mn-cartridges.

2.3. Analysis of ^{226}Ra, ^{228}Ra, and ^{228}Th by Gamma-Ray Spectrometry (Stations 4, 37, and 39)

After the final short-lived Ra isotope RaDeCC analyses were completed (stations 4 and 39) the Mn-cartridges were put into ceramic coffee mugs, covered with a ceramic tile, and placed in a muffle furnace at 820°C for 48 hr. Samples from station 37 were first measured for ^{228}Th ingrowth by RaDeCC (Section 2.5) and then ashed
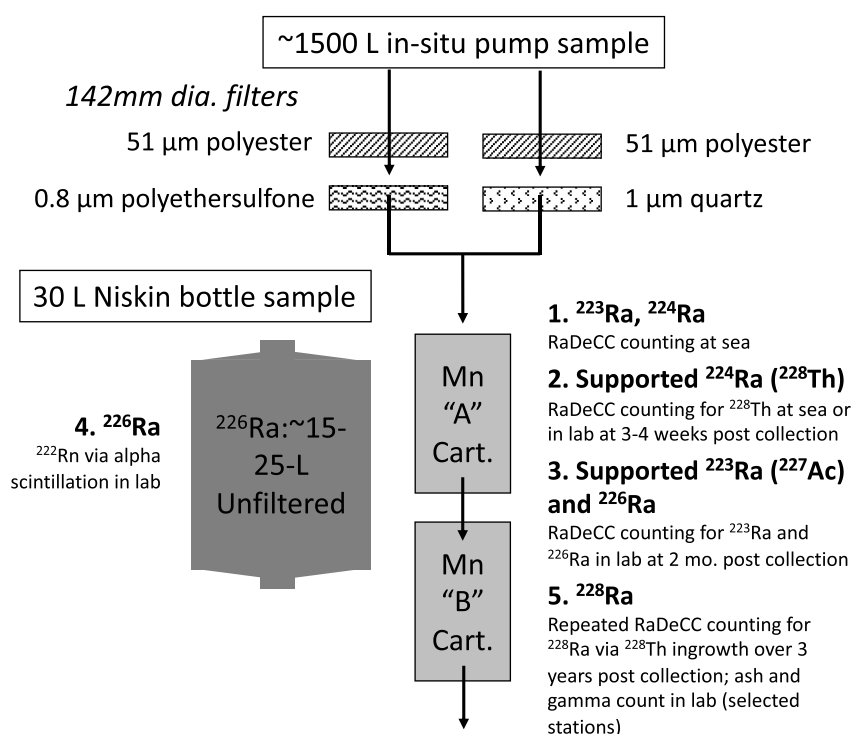
Figure 2. A flow chart illustrating the water column sample collection, processing, and analytical procedures for Ra isotopes. The two streams from the filters were combined before entering cartridge (a) The pump and a flowmeter are downstream of cartridge (b) The water from the Niskin is filtered through a small column of Mn-fiber and the volume recorded.

for gamma measurements. The Mn-cartridge ash was transferred to 15 mm diameter polystyrene vials and sealed with epoxy (to prevent ^{222}Rn loss). Samples were counted for a minimum of one week and a maximum of one month in high purity, well-type germanium detectors at the underground research facility "HADES" in Belgium (Hult et al., 2019, 2020) to quantify ^{226}Ra via the ^{214}Pb photopeak at 352 keV and ^{228}Ra via the ^{228}Ac photopeaks at 338, 911, and 969 keV or by ^{228}Th ingrowth (^{212}Pb photopeak at 238 keV) as described below. The detectors were calibrated using ash prepared from Mn-cartridges soaked in a standard solution containing ^{226}Ra and ^{232}Th (with daughters in equilibrium). Initial ^{228}Th values were derived from the early RaDeCC counts, with the final ^{228}Ra activities determined by multiplying the ^{228}Ra/^{226}Ra on the cartridge ash by the small volume ^{226}Ra measurements on the Mn fiber (SI-1 Text S1 in Supporting Information S1).

2.4. Analysis of ^{232}Th by Gamma-Ray Spectrometry (Core Tops)

A small core was collected at most stations. The core top was sectioned, dried, placed in a counting vial and sealed. The ^{228}Th content of the sample was measured by conventional gamma ray spectrometry at U. SoCal. We assume ^{228}Th was in equilibrium with ^{232}Th.

2.5. Measurement of ^{228}Ra and ^{228}Th by RaDeCC

Because of the large number of samples, it was not possible to measure each sample at the HADES lab. The RaDeCC technique offers another possibility. Here the measurement of ^{228}Ra adsorbed to Mn-cartridges is based on the decay over time of ^{228}Ra to ^{228}Th and its progeny. When the sample is collected it contains both ^{228}Ra and ^{228}Th that were dissolved in seawater. Over time ^{228}Ra decay produces new ^{228}Th while ^{228}Th adsorbed from seawater decreases.

We measured the A cartridge samples 5–6 times over a period of 3 years and applied least squares fit to the data in Microsoft Excel using the Bateman equation (SI-2 Text S2 in Supporting Information S1). The fit provides solutions for ^{224}Ra, ^{228}Th and ^{228}Ra (3×3 matrix). The Excel routine includes a comparison of the fitted or calculated values at each time point as compared to the measured value to quickly identify any obvious outliers.

Generally, any of the 5–6 measured values that deviated from the least squares fit by 50% or more were excluded. Uncertainties were based on the larger of either error propagation of the measured counting uncertainties or the fitting uncertainties. Further details are provided in 2.7 and SI-2 Text S2 in Supporting Information S1.

Because of the different methods used to prepare the Mn-cartridges, the B cartridges often had a higher extraction efficiency than the A cartridges. This sometimes led to a higher ^{226}Ra activity on the B cartridge than the A cartridge even though the B cartridge was behind the A cartridge in the water flow path. We observed that in many cases the sum of ^{226}Ra on the A + B cartridges yielded approximately 100% extraction efficiency. In these cases, we used the sum of ^{228}Ra measured on the two cartridges as the final value and did not correct this based on the ^{226}Ra value for the small volume sample. However, because the B cartridges were usually measured only in 2019 and 2021, we have less confidence in these measurements compared to the A cartridges, which were measured many times (see SI-4 Text S4 in Supporting Information S1). For most samples, we multiplied the ^{228}Ra/^{226}Ra AR measured on the A cartridge by the ^{226}Ra activity in the water column to obtain the ^{228}Ra activity. A table identifying the ^{228}Ra methods used for each station is available in the Supplementary Information (Table SI-1 in Supporting Information S1).

2.6. MATLAB Corrections to RaDeCC Data

During the measurement of samples by RaDeCC, ^{226}Ra on the cartridge produces ^{222}Rn. Although the process is slow (only about 4% of total ^{222}Rn is generated in a 6-hr counting period), the large activity of ^{226}Ra on the cartridge results in a significant increase in the total count rate during the measurement period. As the total count rate increases, the chance coincidence rate increases nonlinearly. We typically correct for chance coincidence counts using equations in Moore and Arnold (1996); however, these are not accurate if the sample has low activity and the chance coincidence count rate, which is increasing during the measurement, is especially high. Hammond (https://github.com/dhammond90290/RadeccMatlab/blob/main/) developed a MATLAB routine for correcting RaDeCC data for chance coincidence counts and other interferences during a measurement period. The routine also assesses leaks and spurious counts. We used this routine to calculate ^{224}Ra and ^{223}Ra from RaDeCC data. For all measurements after 3 weeks of collection ^{224}Ra is a measure of ^{228}Th. The MATLAB routine also supplies a standard deviation or uncertainty of each measurement based on the variance observed for 18 to 30 10-min count intervals, after correction for chance counts (SI-3 Text S3 in Supporting Information S1).

2.7. Uncertainties of the Measurements

For ^{226}Ra from the small volume Mn fiber samples, the average uncertainty (1 sigma) was based on counting statistics of the samples and blanks. For the full data set, relative uncertainties were typically in the 3%–5% range with a maximum of 15.7%.

Standard 1 sigma uncertainties for the four radium isotopes on the Mn cartridges were propagated from the ^{228}Th counting uncertainty (gamma or RaDeCC via the MATLAB routine) and the cartridge scavenging efficiency uncertainty. In the case of excess ^{223}Ra and ^{224}Ra, the uncertainty was propagated from the uncertainties for total ^{224}Ra and ^{228}Th and total ^{223}Ra and ^{227}Ac, respectively. We converted the uncertainty (i.e., stdev) for the ^{228}Th counts into the uncertainty of the calculated initial ^{228}Ra using the following equation:

$$^{228}_i Ra \text{ uncertainty} = \frac{\sqrt{\left(stdev\ ^{228}_m Th\right)^2 + \left(stdev\ ^{228}_i Th * e^{[-\lambda_{Th} t_1]}\right)^2}}{1.499 * \left(e^{[-\lambda_{Ra} t_1]} - e^{[-\lambda_{Th} t_1]}\right)} \tag{1}$$

Here $^{228}_i$Ra is initial ^{228}Ra activity at the time of the first ^{228}Th measurement ($^{228}_i$Th),

$^{228}_m$Th is the measured ^{228}Th activity during the subsequent measurement, t_1 is the elapsed time between measurements, λ_{Th} is the decay constant of ^{228}Th, λ_{Ra} is the decay constant of ^{228}Ra and stdev is the standard deviation of the measurement.

This uncertainty was then propagated with the error on the recovery efficiency to yield the final uncertainty. Because many samples were below the detection limit, we assumed the ^{228}Ra blank was also below the detection level. In cases where we used the A + B cartridge method, we propagated the uncertainties for the ^{228}Ra activity calculated for each cartridge to yield the final uncertainty.
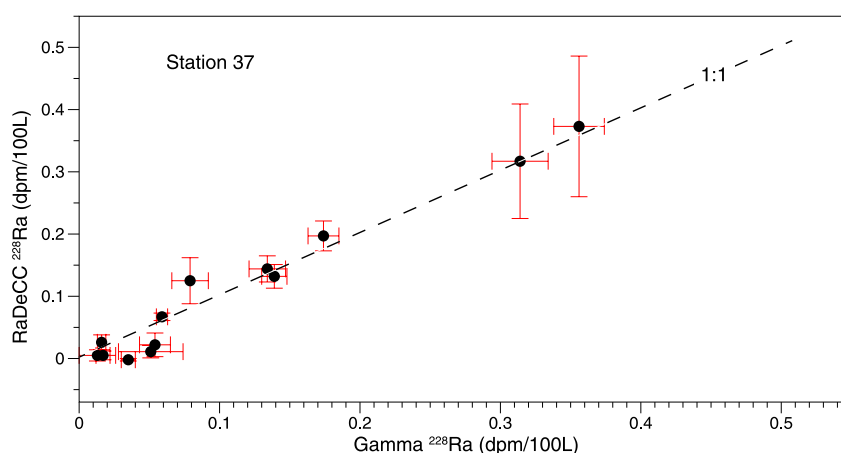
Figure 3. Comparison of ^{228}Ra at station 37 as determined by RaDeCC measurement followed by gamma ray spectrometry. Error bars are 1 sigma. Corrected to time of collection.

For samples measured by gamma ray spectrometry, the ^{228}Ra uncertainty was calculated using Equation 1 propagated with the gamma ^{226}Ra uncertainty and the small-volume ^{226}Ra uncertainty.

Relative uncertainties of ^{228}Ra samples analyzed by gamma averaged 12% while those analyzed on RaDeCC were higher; for both measurements systems, uncertainties typically scale with the reported activity with higher activity samples (e.g., upper ocean and seafloor) having lower relative uncertainties and vice versa.

2.8. Comparison Gamma-Ray Spectrometry Versus RaDeCC Measurements

Samples from station 37 (15°S, 152°W) were analyzed for ^{228}Ra via ^{228}Th ingrowth via RaDeCC followed by gamma ray spectrometry at the HADES underground laboratory in Belgium (Figure 3). For the gamma method, there was generally good agreement between the ^{228}Th ingrowth (^{212}Pb) and direct (^{228}Ra via ^{228}Ac) methods. For gamma versus RaDeCC, there was excellent agreement for samples with >0.1 dpm/100 L, but at lower activities RaDeCC was generally a bit lower than gamma. The ^{228}Ra activities at station 37 were lower than at most other stations.

3. Results

In most cases the activities of excess ^{224}Ra and ^{223}Ra were near or below our detection limit. The notable exception was Station 18.3 at Puna Ridge, where large excesses of ^{223}Ra were measured. At all stations we were able to measure ^{228}Ra activities in shallow and deep samples, and in some cases at intermediate depths. Figure 4 shows the distribution of ^{228}Ra in (a) the upper 800 m and (b) the full water column. Depth profiles at each station are in the Supplementary Information, Figure SI-3 in Supporting Information S1.

3.1. ^{228}Ra in the Upper Water Column (0–800 m)

Figure 4a is a cross section of the ^{228}Ra distribution in the upper 800 m of the water column across the transect. There are three notable enriched zones: Stations 1–4 on the Alaska margin, stations 6–19 between 18° and 52°N, and stations 21–25 between 11° and 5°N.

3.1.1. Alaska Margin

Other than the shelf station (station 1, 95 m bottom depth), with ^{228}Ra activities of 1.0–2.1 dpm/100L (average ~1.6 dpm/100 L), stations closest to the Alaska margin have relatively low ^{228}Ra throughout the water column as compared to stations further to the south (Figure 4a). While there are no prior ^{228}Ra data for the Gulf of Alaska margin, these activities are low in comparison to data from the nearby Bering Shelf (near surface ^{228}Ra = 1.6–12 dpm/100 L, Vieira et al., 2019; 2.1–7.4 dpm/100 L, Kipp et al., 2019) and shelf regions in general (e.g., Charette et al., 2016). Furthermore, there is minimal enrichment of ^{228}Ra near the seafloor (1.0 dpm/100 L) as compared to the Bering Shelf (11–21 dpm/100 L, Kipp et al., 2019). Upper ocean ^{228}Ra values decrease
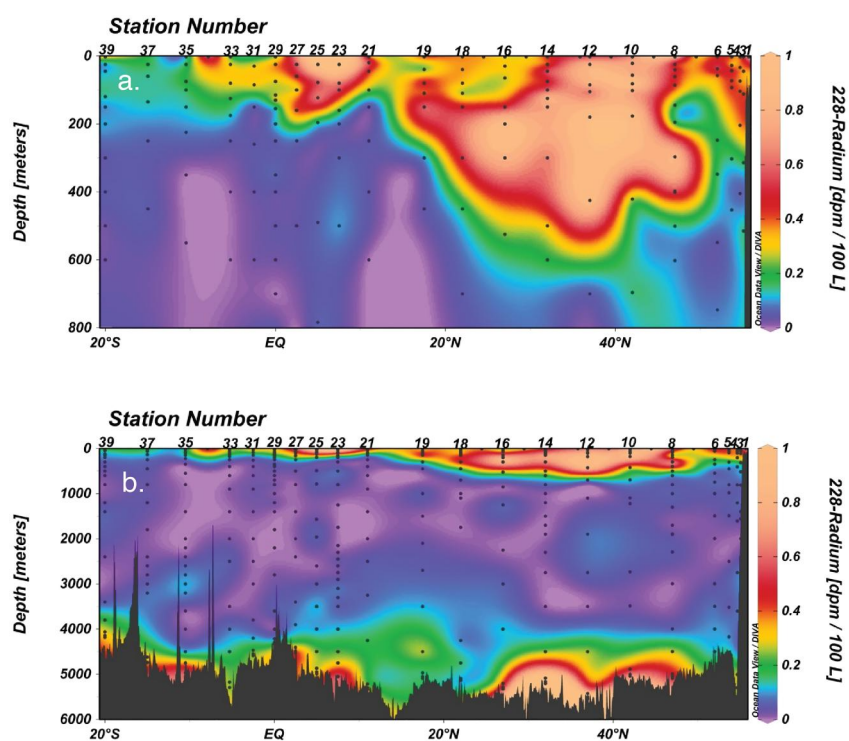
Figure 4. The distribution of ^{228}Ra along the GP15 transect in (a) the upper 800 m (b) the full water column. Units are dpm/100 L.

significantly from station 1 (2 dpm/100 L) to stations 2, 3 and 4, where surface values are ~0.3–0.7 dpm/100 L. Mid-water ^{228}Ra activities are no higher than stations further from the margin, and near bottom values at station 3 on the slope are near or below the detection limit for the 3 samples closest to the seafloor. Samples within ~500 m of the seafloor at station 4 (bottom depth = 5,600 m) were enriched, but low ranging from 0.23 to 0.28 dpm/100 L.

3.1.2. North Pacific (18°–52°N, 152°W)

Relatively high activities of ^{228}Ra (averaging 0.34 to 0.80 dpm/100 L in the upper 100 m) were measured in this region. These stations are within the North Pacific Current (NPC), which transports water west to east. Yamada and Nozaki (1986) and Nozaki et al. (1998) reported ^{228}Ra activities of 2.5–5.9 dpm/100 L near the coast of Japan. These values rapidly decreased to about 1.05 dpm/100 L for samples 500 km offshore (143°E) (SI Figure 1 in Supporting Information S1). The lower ^{228}Ra activities at 152°W compared to these values are consistent with a western source.

High subsurface activities of ^{228}Ra extending to depths of 450 m also occur in this region.

3.1.3. North Equatorial Pacific (2.5°–11°N, 152°W)

Samples collected north of the equator have ^{228}Ra activities of 0.25–1.2 dpm/100 L; these high activities only extend to depths of ~150 m. At similar latitudes but 140°W, Ku et al. (1995) reported somewhat lower activities within this depth range, 0.2 to 0.5 dpm/100 L, suggesting the source of ^{228}Ra enrichment is again from the west.

3.2. ^{228}Ra Within 100 m of the Seabed

Figure 4b is a cross section of the ^{228}Ra distribution for the full water column across the transect. Almost all samples collected within 100 m of the seabed contained measurable ^{228}Ra. In the deep waters, there is one primary enriched area between stations 8–16 from 47° to 27°N, where values within 110 m of the seabed reach 0.4 to 2.1 dpm/100 L. In this region ^{226}Ra values are also high, ranging from 38 to 47 dpm/100 L on both GP15 (Le Roy et al., 2021) and GEOSECS (Chung & Craig, 1980). Slight near bottom ^{228}Ra enrichments occur along 152°W at stations 19 (17.5°N), 23 (7.5°N), 25 (5°N), and 35 to 39 (10°–20°S). Radium-228 anomalies decoupled from the
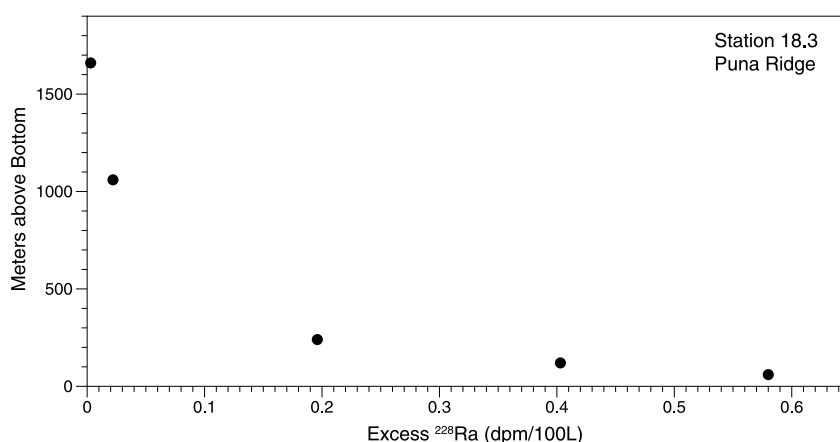
Figure 5. Distribution of ^{223}Ra at Station 18.3, Puna Ridge. Units are dpm/100 L.

seabed were observed at stations 23 (3,100 m), 25 (3,500 m) and 35 (3,000 m); all anomalies are supported by elevated data both above and below the peak values (see depth profiles SI Figure 3).

3.3. ^{223}Ra at Puna Ridge, Station 18.3 (19.68°N, 154.5°W), Depth = 2,160 m

Samples collected on the Puna Ridge within 1,000 m of the seabed contained excess activities of ^{223}Ra (0.05–0.58 dpm/100 L). The activity decreased exponentially away from the seabed (Figure 5). Similar high ^{223}Ra activities were reported at this site by Moore, Ussler, and Paull (2008). The other 3 radium isotopes were not especially enriched at this station.

4. Discussion

The relatively short half-life of ^{228}Ra with respect to ocean-basin scale mixing processes limits its presence in the ocean to water that has had recent (years–decades) contact with ocean boundaries such as continental shelves, slopes, or pelagic sediments (Hammond et al., 1990; Sarmiento et al., 1982). Furthermore, rates of particle uptake and remineralization from the overlying water column are small relative to ^{228}Ra input and decay (Moore, Sarmiento, & Key, 2008). The predominant source of ^{228}Ra to the ocean is ^{232}Th decay in sediments and subsequent exchange between sediment porewater and the overlying water column (Kaufman et al., 1973; Moore, 1969). In shallow waters (up to ~100 m depth), this exchange may occur over short distance scales of cm's, in which case it is referred to as pore water exchange, or over scales of m's, in which case it is referred to as submarine groundwater discharge (SGD) (Moore, 2010). Exchange of ^{228}Ra and ^{226}Ra in the deep sea, except in the case of hydrothermal systems, is thought to occur at the cm scale, driven primarily by bioturbation (Cochran & Krishnaswami, 1980; Kadko et al., 1987). Exchange could be punctuated by turbulent events.

4.1. Near-Surface (0–800 m) Enrichments of ^{228}Ra

4.1.1. Alaska Margin

At the Alaska margin, there exists a relatively steep gradient in surface ^{228}Ra activities between stations 1 (shelf) and 3 (slope), which is indicative of minimal cross shelf transport (Figure 4a). This is likely because the shelf station is within the southwesterly flowing Alaska Coastal Current (ACC), which exists only over the shallow shelf waters, while the slope station intercepts the parallel flowing Alaskan Stream, which is known to entrain water from the deeper Gulf of Alaska (Stabeno et al., 1995).

4.1.2. North Pacific (18°N to 52°N, 152°W) 0–100 m ^{228}Ra Distributions, GP15 and Earlier Measurements

Aside from shelf station 1, the highest upper ocean ^{228}Ra activities on GP15 occurred between 27°N and 52°N, which is within the core of the eastward flowing, large scale North Pacific Current (NPC) (Figure 4a) (Cummins & Freeland, 2007). The ^{228}Ra distribution here is strikingly similar in location and scale to that of ^{134}Cs along 149°E almost one year after the March 2011 Fukushima Dai-ichi nuclear power plant (FDNPP)

Table 1

Calculated Current Speeds From 143°E to Each GP15 Station Setting Initial $^{228}Ra = 1.05$ dpm/100 L as a Line Source and Assuming Only Advection and Decay Control the Decrease of ^{228}Ra

Station	Lat °N	Long °W	Distance (km)	Av ^{228}Ra[a] (dpm/100 L)	U_y (cm s^{-1})
6	52.00	152.00	5,900	0.46	2.7
8	47.00	152.00	5,900	0.53	3.3
10	42.00	152.00	5,900	0.80	8.4
12	37.00	152.00	5,900	0.74	6.6
14	32.00	152.00	5,900	0.48	2.9
16	27.00	152.00	5,900	0.29	1.8

[a]Average ^{228}Ra in Upper 100 m (This Work).

accident (Kumamoto et al., 2014). Buesseler et al. (2017) summarized the spread of the $^{134,137}Cs$ signals into the eastern north Pacific through extensive time series data and modeling. At 150°W they found highest ^{137}Cs activities between 34° and 47°N from 1 to 5 years after the release. Based on the leading edge of the plume, Aoyama et al. (2018) estimated current speeds of 7.8 cm s^{-1} from March 2011 to March 2012 and 3.5 cm s^{-1} from March 2012 through August 2014. These results are consistent with a drifter-based estimate of the horizontal spread of the FDNPP plume (Rypina et al., 2014).

We can couple our data with that of Yamada and Nozaki (1986) and Nozaki et al. (1998) to estimate current speeds of the NPC using ^{228}Ra. Here we use the earlier data for surface water samples that extend from 143°E to 136.3°W (Figure SI-1 in Supporting Information S1) and the equation for the advection of an unstable radionuclide to calculate advection rate. Because of the linearity of the plot (Figure SI-1 in Supporting Information S1) Yamada and Nozaki (1986) only considered advection, not eddy mixing.

$$U_y = \frac{D\lambda}{\ln\left[\frac{A_0}{A}\right]} \tag{2}$$

Where U_y is advection velocity (km yr^{-1}) in the eastward direction, D is distance (km), λ is decay constant of ^{228}Ra (0.121 y^{-1}), A_0 is initial activity at 143°E and A is measured activity. Assuming the system is steady state and ignoring the effects of dilution, Yamada and Nozaki (1986) calculated an average eastward current speed of 5 cm s^{-1} between 500 and 7,300 km off the Japan coast. Their plot gave an intercept at 500 km off the Japan coast of $^{228}Ra = 1.05$ dpm/100 L (SI Figure 1 in Supporting Information S1). We assume (a) an initial activity of 1.05 dpm/100L is a line source 500 km off the Asian coast, (b) steady state conditions, and (c) no dilution to calculate current speeds from 500 km off the Asian coast to each of the GP15 stations (Table 1). The average speed (3.8 cm s^{-1}) is very similar to the offshore velocities reported by Yamada and Nozaki (1986) and Aoyama et al. (2018).

Although this approach is promising, it is prone to large uncertainty. Our estimated NPC speed depends critically on the initial ^{228}Ra activity (A_0) used for the calculation. North of the Yamada and Nozaki (1986) source region, ^{228}Ra activities of 0.6 dpm/100 L were measured by Tazoe et al. (2022). These are not appropriate for our model because the samples were collected at 47°N, within the western Subarctic Gyre (WSAG). This gyre initially transports water westward but turns to the north at ~175°E (Figure 1a: Tazoe et al., 2022) and prevents water from this station reaching further west in the Pacific. The study by Yamada and Nozaki (1986) only considers water samples collected south of 40°N in the region of the NPC. Nevertheless, if we have underestimated A_0, the current speeds would be greater. On the other hand, our estimated NPC speed is less sensitive to higher values for the A_0. For example, the use of 1.5 dpm/100 L, the highest value measured adjacent to the western margin (Fig. S1 in Supporting Information S1), as A_0 reduces our estimate to 1–4 cm s^{-1} for the NPC, which is half our best estimates of 2–8 cm s^{-1}. Another potential source of uncertainty is our neglect of dilution effects while NPC crosses the Pacific. A correction for the dilution effects would cause the true speed to be greater than our estimates at the core of the NPC and smaller at the edges as higher ^{228}Ra water from the core mixes into these regions.

Despite these uncertainties, our estimated zonal velocities are overall consistent with estimates based on the Simple Ocean Data Assimilation (SODA) ocean reanalysis (Carton et al., 2018) (Figure 6). These observations support a northwestern Pacific shelf source carried by the NPC at speeds of 2–7 cm s^{-1} for this near surface ^{228}Ra plume at stations 6–16.
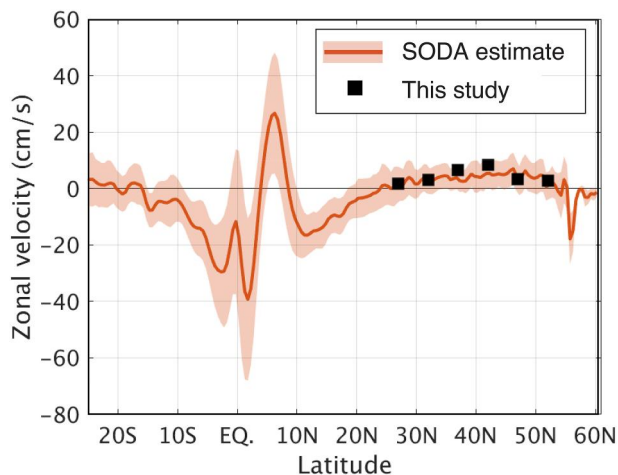

Figure 6. Zonal velocity for near-surface waters at 152°W, taken from SODA v3.3.1. The solid line is the time-average from 1980 to 2015 and the shade represents a standard deviation of the monthly mean data. Our estimates are shown in black squares. SODAv3.3.1 is available at http://apdrc.soest.hawaii.edu/datadoc/soda_3.3.1.php.
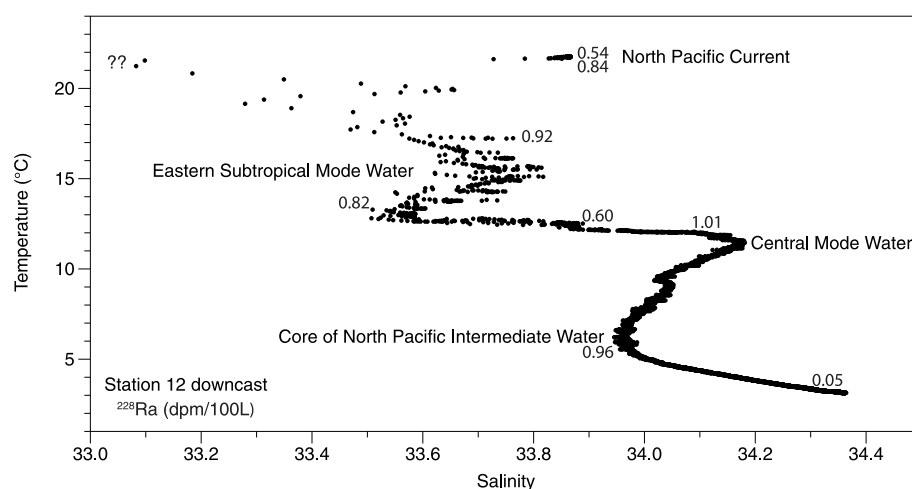
Figure 7. Upper (0–1,000 m) water column profile of temperature and salinity at Station 12 (37°N, 152°W). The water masses are identified and ^{228}Ra activities (dpm/100 L) are indicated.

4.1.3. North Pacific (18°N to 52°N, 152°W) 200–450 m ^{228}Ra Distributions

In addition to the near surface enrichment, there is a subsurface ^{228}Ra maximum (200 m; Figure 4a) between 18 and 47°N that is probably associated with Central Mode Water (CMW, Hautala & Roemmich, 1998). Samples at this depth and latitude were also enriched in FDNPP-derived ^{134}Cs (Kumamoto et al., 2014), again indicating a substantial advection velocity. Below the CMW is the North Pacific Intermediate Water (NPIW, You, 2003), which shows up as a salinity minimum and contains high ^{228}Ra activity. It is thought that the NPIW originates as water from the Sea of Okhotsk spills over a deep ridge and mixes with a subtropical component of the Kuroshio (You, 2003). Figure 7 is a T-S diagram at station 12 (0–1,000 m) with water masses and ^{228}Ra activities indicated.

4.1.4. North Equatorial Pacific (2.5°–11°N, 152°W) ^{228}Ra Distributions

The near surface ^{228}Ra enrichments between 2.5° and 11°N are associated with the North Equatorial Countercurrent (NECC), which originates in the far western Pacific (Zhou et al., 2021) and is well known to transport trace metals of terrigenous origin from the western Pacific margin to the eastern tropical North Pacific Ocean (Gordon et al., 1997; Slemons et al., 2012). SODA estimated the average velocity of the NECC centered at ~6°N exceeds 20 cm s^{-1} (Figure 6). Although we do not have initial ^{228}Ra activities to calculate current speeds, our highest ^{228}Ra activities in this region (1.1–1.2 dpm/100 L) bisect this peak speed at stations 25 (7.5°N) and 23 (5° N), indicating very rapid movement of the enriched plume from its origin. The ^{228}Ra distribution is broadly consistent with an upper ocean ^{228}Ra section along 140°W (Ku et al., 1995) and with the modeling work of Kwon et al. (2014), which calls for a substantial margin source of ^{228}Ra from southeast Asia to the Equatorial North Pacific Ocean (Charette et al., 2016).

4.1.5. Inventories of ^{228}Ra in the Upper Ocean (0–800 m)

Most stations sampled 6–12 depths in the upper 800 m of the water column. This is sufficient to calculate the inventory of ^{228}Ra in this depth range across the transect using simple integration between each depth increment. In cases of pump failure or low yield, activities at specific depths were estimated based on adjacent samples. For samples within 50 m of 800 m, this value was used for 800 m; if there was no sample within 50 m of 800 m, the activity at 800 m was estimated based on adjacent samples. We recognize these integrations are somewhat crude because they assume a consistent change with depth as we average samples from adjacent depths. Figure 7 is a good example of how such integrations may not fully capture the complexity. Here we focus on the broad picture as revealed in Figure 8. The peak centered on 37°N stands out clearly, indicating the flow in the upper 800 m from the Asian margin is focused near this latitude.

Fröllje et al. (2016) reported inventories of ^{228}Ra to 500 m at Station Aloha (22°45'N, 158°W, ~100 km north of Oahu, Hawaii) of 7,590 dpm m^{-2} and on a transect ~15 km off Oahu of 9,450 dpm m^{-2}. The Aloha station and the
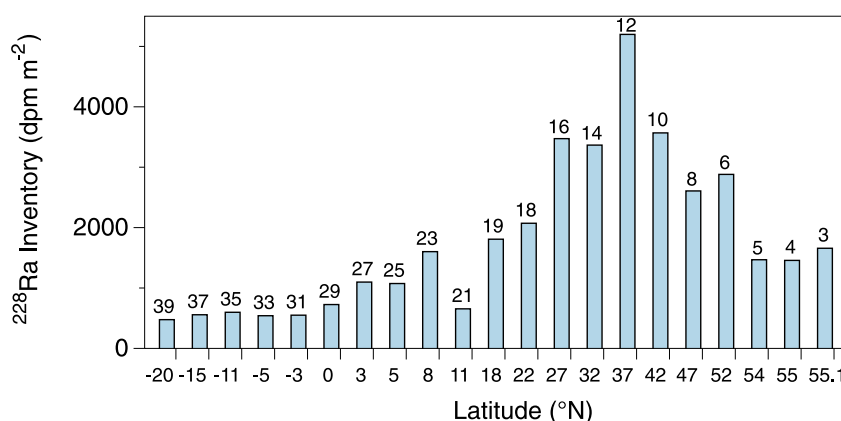
Figure 8. Inventories (dpm m^{-2}) of ^{228}Ra in the upper ocean (0–800 m). Station numbers are above the bars. Because of unknown uncertainties in the integration procedure, we have not estimated uncertainties.

transect are relatively close to Station 18 (22°N, 152°W) where we measured a much lower ^{228}Ra inventory (adjusted to 500 m depth) of 1,760 dpm m^{-2}, indicating a ^{228}Ra flux from the Hawaiian Islands is increasing the ^{228}Ra inventories closer to Hawaii.

The higher inventories in the North Pacific relative to the South Pacific (Figure 8) are consistent with the greater proportion of shelf area in the Northern Hemisphere; this pattern was also observed in the North versus South Atlantic Ocean (Charette et al., 2015; Moore, Sarmiento, & Key, 2008). There are not enough vertical ^{228}Ra profiles in the upper Indian Ocean to construct inventories for this basin.

4.1.6. Comparison of ^{228}Ra in Upper (0–800 m) Pacific to Atlantic and Indian Oceans

The ^{228}Ra upper ocean inventories (0–800 m) at 152°W range from ∼500 to ∼5,000 dpm/m^2 (Figure 8). The average inventories on GP15 (1,780 dpm m^{-2}) are about six times lower than upper Atlantic Ocean inventories (10,600 dpm m^{-2}, Moore, Sarmiento, & Key, 2008; Charette et al., 2015). These differences are due to (a) the larger surface area of the Pacific Ocean, (b) the lower area of continental shelf in the Pacific where near-surface waters are in direct contact with sediments, and (c) differences in submarine groundwater discharge, including different ^{228}Ra end-member concentrations between the two oceans (Kwon et al., 2014).

Global ocean models provide an excellent way to compare the distribution of ^{228}Ra in different oceans. The application of such models to ^{228}Ra distributions was pioneered by Kwon et al. (2014). They used detailed vertical profiles of ^{228}Ra from the Atlantic Ocean to tune the model for this basin and then extended the model to include other basins based on surface ^{228}Ra measurements. We now use GEOTRACES ^{228}Ra measurements to update the Kwon model to provide a detailed visual picture of the near-surface (18 m) distribution of ^{228}Ra. Figure 9 consists of three maps of the distribution of ^{228}Ra at a depth of 18 m for the world ocean shown at different scales. Because the surface ^{228}Ra is highly skewed on a global scale with a skewness of 0.96, different linear scales highlight different aspects of surface ocean ^{228}Ra distributions. The 0–5 dpm/100 L linear scale with a 0.5 dpm/100 L increment (Figure 9a) recognizes only the Pacific shelf regions and a slight enrichment in the Eastern Equatorial Current. These small regions compare with large Indian Ocean enrichments at this scale in the Arabian Sea, Bay of Bengal, Indonesian archipelago, western equatorial current off Australia, and coasts of South Africa and Madagascar. Atlantic enrichments at this scale appear in the Caribbean Sea, Gulf of Mexico, Gulf of St. Lawrence, and east coast of North America. Most of the Arctic Ocean is also enriched at this scale. At the 0 to 3 dpm/100 L scale with a 0.3 dpm/100 L increment (Figure 9b), the Eastern Equatorial Current and the NPC appear in the Pacific, while much of the Indian Ocean exceeds the upper range of 3 dpm/100 L. At this scale the Atlantic Equatorial Current and the North America and Mediterranean margins reveal their significance. At the lowest color saturation limit of 1 dpm/100 L with a 0.1 dpm/100 L increment (Figure 9c), the Pacific Eastern Equatorial Current and the NPC are well defined, but the South Pacific remains largely a void. At this scale most of the Indian and Atlantic Oceans are color saturated, except for the eastward-flowing branch of the Brazil Current off southern Brazil and Argentina.
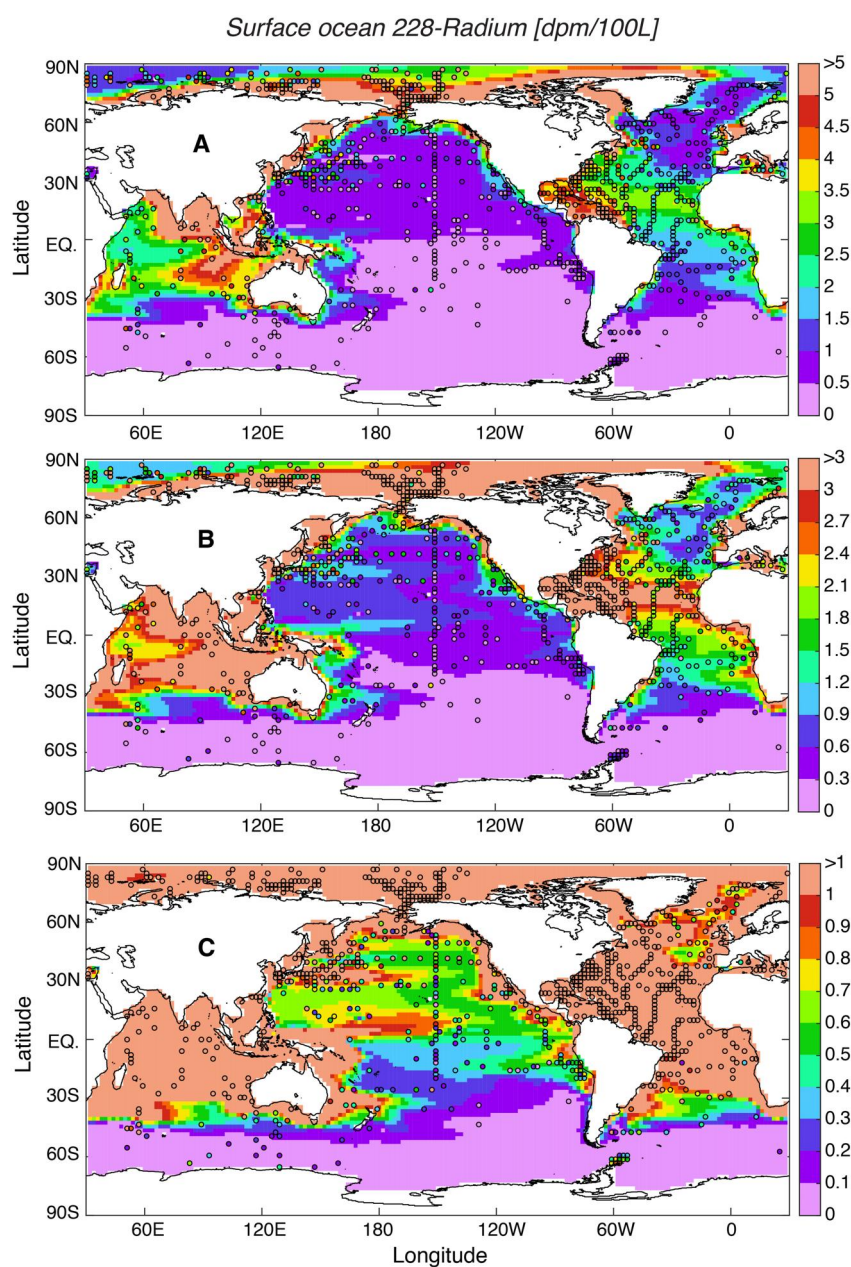
Figure 9. Three World Ocean maps are based on the integration of near-surface (18 m) distributions of ^{228}Ra measured over the past 6 decades with a global ocean model (Kwon et al., 2014, plus GP15 data). These maps are shown at different scales to demonstrate the differences in ^{228}Ra in different oceans and emphasize how ocean circulation features are reflected in the ^{228}Ra abundances (a) At a scale of 0–5 dpm/100 L the Pacific Ocean is almost devoid of prominent features which are well-resolved in the Indian and Atlantic Oceans (b) At a scale of 0–3 dpm/100 L the outlines of some features in the Pacific Ocean become apparent as does the Equatorial Current system in the Atlantic (c) The lowest scale, 0–1 dpm/100 L is required to clearly define features in the Pacific Ocean, while ^{228}Ra activities in the Indian and Atlantic Oceans are largely color saturated at >1 dpm/100 L.

4.2. Benthic ^{228}Ra Water Column Distributions

4.2.1. Measured ^{228}Ra Near-Bottom (0–~100 m Above Bottom) Distribution on GP15

Distributions of ^{228}Ra in deep waters are due almost entirely to sediment fluxes, water mixing, and decay. Here we focus on the distributions within 100 m of the seabed to reduce the effects of horizontal mixing and decay and therefore emphasize the importance of local fluxes. For all but six deep-water stations on GP15, 2 samples within
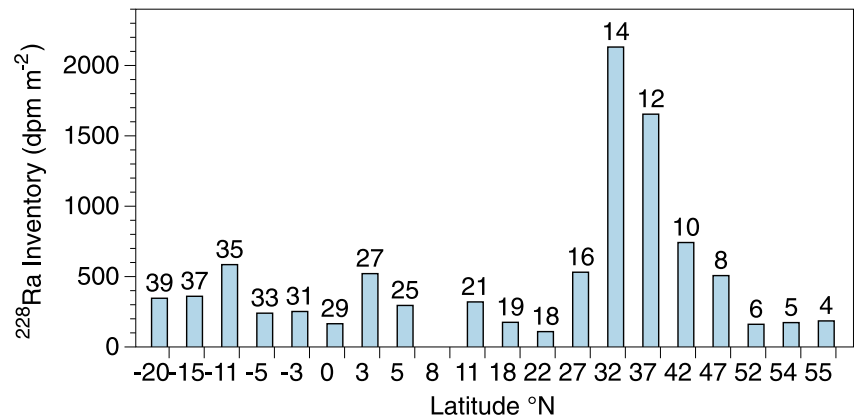
Figure 10. The inventories of ^{228}Ra (dpm m^{-2}) within 100 m of the seabed along GP15. Station numbers are above each bar. There were no samples within 110 m of the seabed at station 23 (8°N). Because of unknown uncertainties in the integration procedure, we have not estimated overall uncertainties.

110 m of the bottom were averaged to obtain a mean activity in this region. For the single sample stations, this result was assumed to represent the 0–100 m activity. One station (29) had no samples within 110 m of the bottom. Activities were converted to inventories (dpm m^{-2}) within 100 m of the seabed. Figure 10 shows the distribution of bottom ^{228}Ra inventories along GP15. The primary ^{228}Ra enriched area shown in Figure 4b between stations 8–16 (47°–27°N), is shown clearly here. Near-bottom ^{228}Ra inventories average 1,110 dpm m^{-2} for stations 8–16 but only 280 dpm m^{-2} for the other stations. Stations 8–16 are also strongly enriched in ^{226}Ra (Le Roy et al., 2021).

The high inventories at stations 12 and 14 appear to be from the same source based on Figure 11, a plot of ^{228}Ra versus sigma-theta. The similar distributions for stations 12 and 14 imply near-isopycnal mixing of an enriched endmember near station 14 with more dilute (older?) water. Near-bottom samples from adjacent stations (8 and 10) also plot within this narrow sigma-theta range but are not as enriched in ^{228}Ra. These high ^{228}Ra activities are not due to release from suspended particulate matter. Bottom water lithogenic particle concentrations at station 14 are <5 μg/L (Lanning et al., 2023). If the suspended lithogenic particles have the same average ^{232}Th as the bottom sediments (~2 dpm/g, Figure 12), the suspended particle activity would be 0.001 dpm/100 L, <0.1% of measured ^{228}Ra.
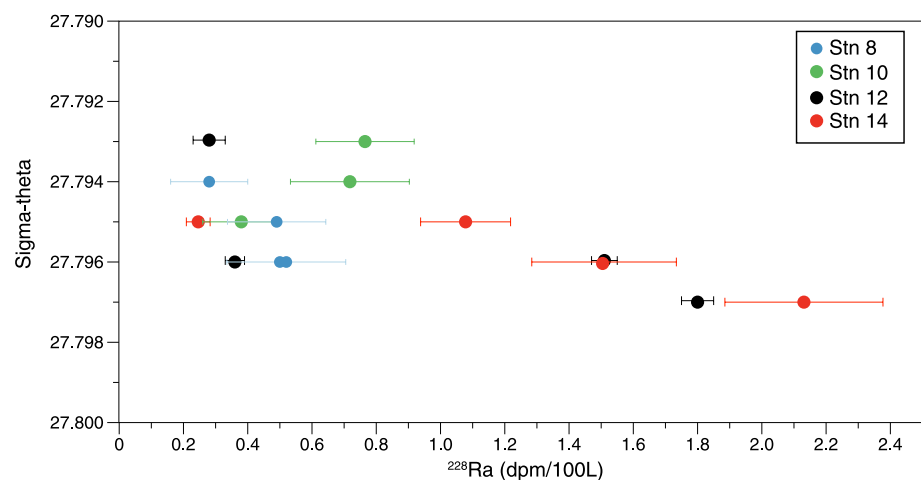

Figure 11. A plot of ^{228}Ra versus sigma-theta for the near-bottom samples (>4,000 m depth) at stations 8–14 implies near-isopycnal mixing of ^{228}Ra in these bottom waters.
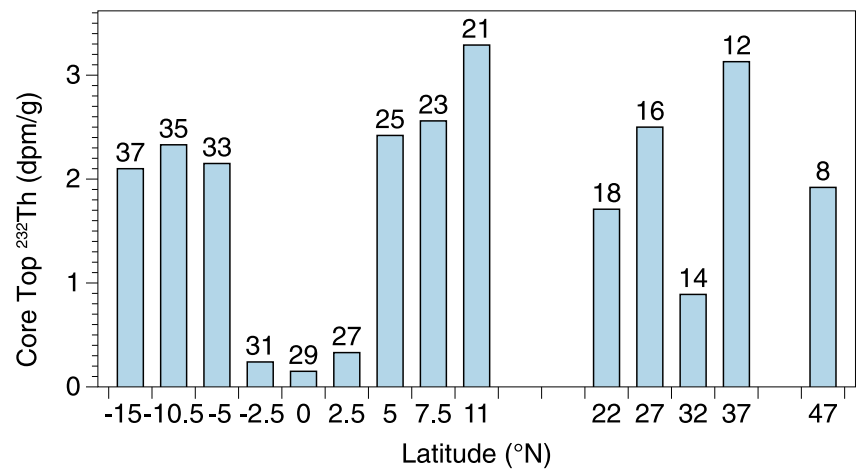
Figure 12. Activities of ^{232}Th (dpm/g) in core top sediments based on gamma ray spectrometry, assuming equilibrium between ^{228}Th and ^{232}Th in these samples. Station numbers are above each bar. There were no samples at stations 4, 10, 19, or 39. The low values near the equator reflect the presence of calcium carbonate containing low ^{232}Th. Surprisingly, the high ^{228}Ra inventories at station 14 do not coincide with high ^{232}Th in the sediments, indicating other factors can play a significant role in controlling the ^{228}Ra inventory.

4.2.2. Estimated Benthic ^{228}Ra Fluxes

Four primary factors affect bottom fluxes of ^{228}Ra (Cochran & Krishnaswami, 1980; Kemnitz et al., 2022). (a) Higher upper ocean productivity will deposit more organic carbon on the seabed and stimulate bioturbation, leading to ^{228}Ra release. (b) Accumulation of opal and calcite will dilute the ^{232}Th content of the sediment, leading to lower fluxes. (c) The position of ^{232}Th in the mineral lattice determines the fraction of ^{228}Ra produced upon decay that is mobile. (d) Superimposed on these variables is radium adsorption to solid phases, which will reduce ^{228}Ra fluxes. In general, we expect adsorption onto barite to be highest followed by clay, opal, and calcite. The Mn content of the sediment also plays a major role in adsorbing radium (Kemnitz et al., 2022). These primary factors could be augmented by episodic erosional or depositional events. It is a complicated system, one for which we have little data on the relative importance of different processes.

Factor (b) can be evaluated in this study. The ^{232}Th activities in the sediments range from 0.15 to 3.3 dpm g^{-1} based on gamma ray spectrometry, assuming equilibrium between ^{232}Th and ^{228}Th (Figure 12). The low values near the equator reflect the dominance of calcium carbonate containing low ^{232}Th. The near-bottom ^{228}Ra inventories do not reflect the ^{232}Th content of core top sediments collected at most of the other stations. In fact, station 14 has the highest dissolved ^{228}Ra inventories but the lowest core top ^{232}Th activity (excluding the equatorial stations). This could be partially but not entirely explained by ^{228}Ra loss from the sediments, yielding ^{232}Th activities that are too low.

4.2.3. Comparing Estimated Benthic ^{228}Ra Fluxes With 0 to +1,000 m Water Column Inventories

Kemnitz et al. (2022) evaluated ^{226}Ra, ^{228}Ra and ^{227}Ac fluxes for 5 cores collected close to the GP15 transect from 23°N to 50°N, near our region of highest ^{228}Ra benthic inventories. These flux estimates were based on (a) reaction-transport modeling of depth profiles of solid phase measurements, (b) integrated profiles of daughter-parent deficiencies, and (c) directly measuring fluxes from incubated cores, that is, measuring changes in time (1,200 days) of ^{228}Ra activity in waters overlying the cores. This straightforward method yielded fluxes of 390–880 dpm m^{-2} yr^{-1} for 5 cores, with analytical uncertainty of 25%–58%. These fluxes translate to total ^{228}Ra inventories of 3,250–7,300 dpm m^{-2}. The highest ^{228}Ra flux was located at 35.3°N, 151°W, near station 14, with decreasing fluxes to the south and north. These estimates are remarkably similar to results of Cochran and Krishnaswami (1980), who measured ^{228}Ra fluxes from 3 north equatorial Pacific cores to be 400, 600, and 800 dpm m^{-2} yr^{-1}.

Most of the benthic inventory of ^{228}Ra is trapped in the lower 1,000 m of the water column (Figure 4b). To compare GP15 inventories with the Kemnitz fluxes, we have extended the range of our inventory calculations to

Table 2
Inventory (I) Calculations of ^{228}Ra From 0 to +100 m and 0 to +1,000 m From the Seabed for Stations 6–16

Station	Latitude °N	^{228}Ra I dpm m^{-2} 0 to +100 m	^{228}Ra I dpm m^{-2} 0 to ~+1,000 m	I_{100}/I_{1000}
6	52	161	2,016	0.08
8	47	507	3,433	0.15
10	42	742	3,439	0.22
12	37	1,654	5,190	0.32
14	32	2,131	6,700	0.32
16	27	531	4,138	0.13
			Average	**4,150**

Note. I_{100}/I_{1000} is the ratio of the 0–100 m and 1–1,000 m inventories. The average value of the 0–1,000 m inventory is 4,150.

+1,000 m from the seabed for stations 6–16, corresponding to the Kemnitz stations at 23°–50°N. We caution that assigning total inventories (0 to +1,000 m) to specific stations is only qualitative because the ocean is not one-dimensional on the time scale of the ^{228}Ra mean life (8.3 years), and horizontal transport is likely significant (Sarmiento et al., 1982). Here the range of inventories is more important than specific values (Table 2).

The ^{228}Ra fluxes estimated by Kemnitz et al. (2022) would produce inventories ranged from 3,250–7,300 dpm m^{-2}. The measured range of inventories (2,000–6,700 dpm m^{-2}) is somewhat lower than predicted. This is not surprising because the ^{228}Ra source in this region is greater than in adjacent regions (Figure 4b); therefore, the signal will mix with water containing lower ^{228}Ra and decrease the inventory in this region. Thus, the ^{228}Ra fluxes are entirely adequate to support the inventories.

It is instructive to compare the inventories in the 0–100 m range (I_{100}) with the 0–1,000 m range (I_{1000}). The I_{100}/I_{1000} ratio is highest at stations 12 and 14, where the 0–100 m inventories are unusually high. We consider this evidence that about a third of the ^{228}Ra released from the sediments is trapped near the seabed in this region. This is a region of the Pacific where deep circulation is a minimum. As Hautala (2018) has pointed out: "This region has very weak diapycnal and lateral mixing, and an aspect ratio for the overturning circulation that is correspondingly flat, with bottom water parcels rising less than 1 km during their long transit from the Aleutian Trench to the latitude of Hawaii." We conclude that the measured fluxes and sluggish circulation lead to the build-up of high ^{228}Ra activities in the near-bottom waters at stations 12 and 14.

Pacific GEOSECS found the highest ^{226}Ra values ever measured in the ocean at that time in bottom waters at their nearby station 204 (31.38°N., 150.03°W, 5,292 m depth, Chung & Craig, 1980). Our measurements of ^{226}Ra at station 14 agreed with the GEOSECS results (Le Roy et al., 2021). The ^{226}Ra distribution also reflects a strong bottom source with sluggish circulation.

4.2.4. Intermediate Water (1,000–3,500 m Depth) ^{228}Ra Activities

The ^{228}Ra activity in most intermediate waters (1,000–3,500 m depth) was below our detection limit of ~0.1 dpm/100 L. Some ^{228}Ra anomalies were observed in deep waters from 1,500 to 2,000 m above the local seabed (Figure 4b). These could be explained by inputs from nearby topographical features such as seamounts (Kipp et al., 2015; Neuholz et al., 2020). We see no convincing evidence for hydrothermal inputs of ^{228}Ra to intermediate waters.

4.2.5. Comparison of ^{228}Ra in Benthic (0 to +100 m Depth) Pacific and Atlantic

Distributions of ^{228}Ra in deep Atlantic waters were measured during the Transient Tracers in the Ocean (TTO) project (Key et al., 1990, 1992a, 1992b) and during GA03 (Charette et al., 2015). Here (Figure 13) we show a comparison between the inventories within 100 m of the seabed in the Atlantic (GA03) and Pacific (GP15) as a function of water depth. The Atlantic TTO data (Key et al., 1990, 1992a, 1992b) have near-bottom inventories similar to GA03. Pacific stations 12 and 14 stand out as having the highest inventories in either basin. Excluding these stations, the average Atlantic inventories (630 dpm m^{-2}) are almost twice the average Pacific inventories (330 dpm m^{-2}). We think stronger near-bottom currents in the Atlantic relative to the Pacific (Hautala, 2018) should carry ^{228}Ra further away from the bottom in the Atlantic thereby decreasing the near-bottom inventory The higher prevalence of carbonate sediments (low ^{232}Th) in the Atlantic should also lead to lower Atlantic near-bottom inventories. Sediment bioturbation certainly plays a role the ^{228}Ra benthic flux (Kemnitz et al., 2022). Middelburg et al. (1997) have shown that sediment bioturbation decreases with increasing water depth. Since the Pacific is about 10% deeper than the Atlantic, this suggests the Pacific should have lower bioturbation. However, depth does not appear to control ^{228}Ra inventories shown on Figure 13. For example, Atlantic stations at 4,500 ± 200 m have over twice the ^{228}Ra inventory compared to Pacific stations in this depth range. There may be other factors such as the flux of organic carbon and the manganese content of the sediments (Kemnitz et al., 2022) that we are unable to evaluate. We cannot explain why ^{228}Ra inventories are lower in the Pacific.
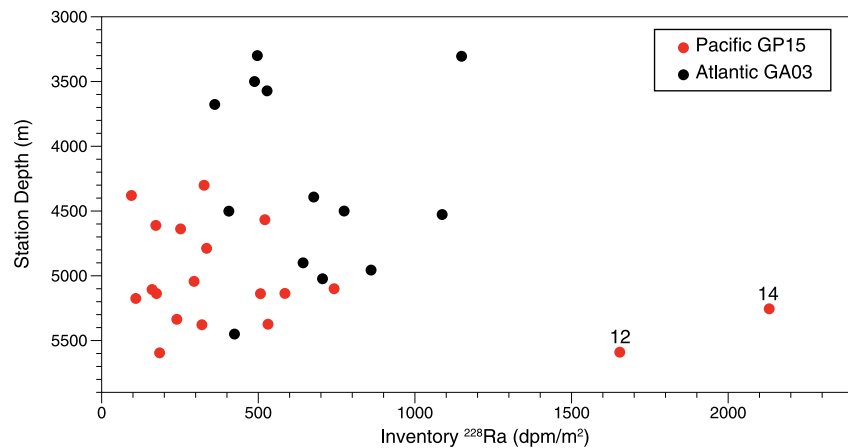
Figure 13. Inventories of ^{228}Ra (dpm m^{-2}) within 100 m of the seabed in deep Pacific (red, GP15) and Atlantic (black, GA03) waters. GP15 stations 12 and 14 are indicated. Atlantic data from Charette et al. (2015).

5. Enriched ^{223}Ra Above Puna Ridge Near Hawaii

The 75 km long Puna Ridge is the East Rift Zone of the Kilauea Volcano, Hawaii. Strong thermal signals and high activities of ^{223}Ra were measured 1–3 m above the Puna Ridge by an ROV in 2001, indicating seawater was flowing through this structure (Moore, Ussler, & Paull, 2008). Station 18.3 reoccupied the site of these previous measurements. Like the samples collected in 2001, these samples contained high activities of ^{223}Ra, with an exponential decrease near the bottom (Figure 5). The activities of ^{226}Ra were similar to nearby stations; ^{228}Ra was near the detection limit, and excess ^{224}Ra was below detection.

We have subtracted supported ^{227}Ac activities of 0.1 dpm/100 L for the 3 deepest samples (Kemnitz et al., 2022) to yield excess ^{223}Ra values. The deepest sample, which was 60 m above the ridge contained 0.58 dpm/100 L; the 2,001 samples collected 1–3 m above the ridge contained 0.8 to 1.9 dpm/100 L. If we assume a 1-D mixing model without advection, we can relate the GP15 excess ^{223}Ra distribution to a vertical mixing rate (K_z).

$$A_z = A_0 \exp\left[-z\sqrt{\frac{\lambda}{K_z}}\right] \qquad (3)$$

where Az is the measured excess ^{223}Ra activity z meters above bottom, A_0 is initial ^{223}Ra, λ_{223} is the ^{223}Ra decay constant (0.0608 d^{-1}). The term (λ_{223}/K_z) is obtained by plotting measured ln ^{223}Ra as a function of distance above bottom (see SI Figure 2 in Supporting Information S1). Because ^{223}Ra in samples collected more than a few hundred meters above bottom may be diluted by horizontal mixing, we restrict our data set to 3 samples collected within 120 m of the bottom. The slope of the line (−0.00603) is the square root of (λ/K_z). Solving for K_z yields a vertical mixing rate of 0.019 m^2 s^{-1}.

This is somewhat greater than average K_z values of 0.0002–0.005 m^2 s^{-1} based on Pacific ^{222}Rn profiles (Ku & Luo, 2008), but not surprising considering the heat flux from Puna Ridge (Moore, Ussler, & Paull, 2008).

The lowest three points (Figure 5) could alternately be interpreted as a linear decrease. In this case we would use Equation 2 to yield a vertical advection rate of 1.2×10^{-4} m s^{-1}.

6. Conclusions

Using repeated RaDeCC measurements of ^{228}Ra, which were verified by very low background gamma spectrometry measurements at an underground lab, we established the ^{228}Ra distribution along the GP15 transect from Alaska to Tahiti at 152°W. The transect encountered several regions where ^{228}Ra was significantly enriched. These include stations 1–4 on the Alaska margin, which is sourced locally but the enrichment does not extend to the Alaskan trench at station 5.

The North Pacific Current (NPC) carries substantial ^{228}Ra to the central north Pacific (27°–52°N) from the Asian margin at current speeds of 2–8 cm/s as determined by a ^{228}Ra advection model which agreed with other methods. This area is underlain by a subsurface enrichment (200–400 m) from 18°N to 47°N, which is associated with Central Mode Water around 200 m and North Pacific Intermediate Water at 450 m. Further south, the near-surface North Equatorial Countercurrent (NECC) also carries high ^{228}Ra activities from the Asian margin to an enriched region between 5° and 11°N. Overall, ^{228}Ra activities in the upper Pacific are six times lower than activities in the upper Atlantic.

In deep waters the primary zone of ^{228}Ra enrichment is between 27° and 47°N. Near-bottom inventories (0–100 m above the seabed) for these stations average four times greater than the other stations on GP15. We attribute the high near-bottom ^{228}Ra at stations 12 and 14 to sluggish circulation in this region, leading to long water residence times and ^{228}Ra build-up. Benthic fluxes of ^{228}Ra measured at nearby stations (Kemnitz et al., 2022) estimate ^{228}Ra inventories somewhat greater than measured inventories between 27° and 47°N. We attribute this to the dilution of ^{228}Ra in this high-source region by lower ^{228}Ra activities away from the source. Excluding stations 12 and 14, the remaining Pacific stations average almost 50% lower near-bottom ^{228}Ra inventories than average Atlantic stations; we cannot explain why.

Station 18.3 confirmed one region of enriched ^{223}Ra (half-life = 11 days) above the Puna Ridge near Hawaii. We measured similar ^{223}Ra activities in the water column and estimated a vertical mixing rate of 0.019 $\text{m}^{-2}\,\text{s}^{-1}$ at this site.

The ^{228}Ra data should provide constraints regarding sources and timescales controlling other TEI distributions. We plan to couple the ^{228}Ra measurements with other reported TEI data to gain insights regarding the sources and fluxes of these TEIs. We encourage other investigators to consider the constraints the ^{228}Ra data place when interpreting additional GP15 data sets.

Conflict of Interest

The authors declare no conflicts of interest relevant to this study.

Data Availability Statement

The data on which this article is based have been deposited at BCO-DMO: https://www.bco-dmo.org/dataset/825891 and https://www.bco-dmo.org/dataset/825947. The MATLAB code for correcting RaDeCC data is in the GitHub repository https://github.com/dhammond90290/RadeccMatlab/blob/main/. The surface current speeds from SODAv3.3.1 are available at http://apdrc.soest.hawaii.edu/datadoc/soda_3.3.1.php.

References

Anderson, R. F. (2020). GEOTRACES: Accelerating research on the marine biogeochemical cycles of trace elements and their isotopes. *Annual Review of Marine Science*, *12*(1), 49–85. https://doi.org/10.1146/annurev-marine-010318-095123

Aoyama, M., Hamajima, Y., Inomata, Y., Kumamoto, Y., Oka, E., Tsubono, T., & Tsumune, D. (2018). Radiocaesium derived from the TEPCO Fukushima accident in the North Pacific ocean: Surface transport processes until 2017. *Journal of Environmental Radioactivity*, *189*, 93–102. https://doi.org/10.1016/j.jenvrad.2018.03.014

Broecker, W. S., & Peng, T.-H. (1982). *Tracers in the Sea*. Lamont-Doherty Geological Observatory, Columbia University Palisades.

Buesseler, K., Dai, M., Aoyama, M., Benitez-Nelson, C., Charmasson, S., Higley, K., et al. (2017). Fukushima Daiichi–derived radionuclides in the ocean: Transport, fate, and impacts. *Annual Review of Marine Science*, *9*(1), 173–203. https://doi.org/10.1146/annurev-marine-010816-060733

Carton, J. A., Chepurin, G. A., & Chen, L. (2018). SODA3: A new ocean climate reanalysis. *Journal of Climate*, *31*(17), 6967–6983. https://doi.org/10.1175/jcli-d-18-0149.1

Charette, M. A., Kipp, L. E., Jensen, L. T., Dabrowski, J. S., Whitmore, L. M., Fitzsimmons, J. N., et al. (2020). The Transpolar Drift as a source of riverine and shelf-derived trace elements to the central Arctic Ocean. *Journal of Geophysical Research: Oceans*, *125*(5), e2019JC015920. https://doi.org/10.1029/2019JC015920

Charette, M. A., Lam, P. J., Lohan, M. C., Kwon, E. Y., Hatje, V., Jeandel, C., et al. (2016). Coastal ocean and shelf-sea biogeochemical cycling of trace elements and isotopes: Lessons learned from GEOTRACES. *Philosophical Transactions of the Royal Society A Math, Physics, Engineering Science*, *374*(2081), 20160076. https://doi.org/10.1098/rsta.2016.0076

Charette, M. A., Morris, P. J., Henderson, P. B., & Moore, W. S. (2015). Radium isotope distributions during the US GEOTRACES North Atlantic cruises. *Marine Chemistry*, *177*, 184–195. https://doi.org/10.1016/j.marchem.2015.01.001

Charette, M. A., & Scholten, J. C. (2008). Marine Chemistry special issue: The renaissance of radium isotopic tracers in marine processes studies. *Marine Chemistry*, *109*(3–4), 185–187. https://doi.org/10.1016/j.marchem.2008.04.001

Chung, Y. (1980). Radium-barium-silica correlations and a two-dimensional radium model for the world ocean. *Earth and Planetary Science Letters*, *49*(2), 309–318. https://doi.org/10.1016/0012-821x(80)90074-6

Chung, Y., & Craig, H. (1980). ^{226}Ra in the Pacific Ocean. *Earth and Planetary Science Letters*, *49*(2), 267–292. https://doi.org/10.1016/0012-821x(80)90072-2

Cochran, J. K., & Krishnaswami, S. (1980). Radium, thorium, uranium, and ^{210}Pb in deep-sea sediments and sediment pore waters from the North Equatorial Pacific. *American Journal of Science*, *280*(9), 849–889. https://doi.org/10.2475/ajs.280.9.849

Cummins, P. F., & Freeland, H. J. (2007). Variability of the North Pacific current and its bifurcation. *Progress in Oceanography*, *75*(2), 253–265. https://doi.org/10.1016/j.pocean.2007.08.006

Diego-Feliu, M., Rodellas, V., Alorda-Kleinglass, A., Tamborski, J., van Beek, P., Heins, L., et al. (2020). Guidelines and limits for the quantification of Ra isotopes and related radionuclides with the radium delayed coincidence counter (RaDeCC). *Journal of Geophysical Research: Oceans*, *125*(4), e2019JC015544. https://doi.org/10.1029/2019jc015544

Fröllje, H., Pahnke, K., Schnetger, B., Brumsack, H.-J., Dulai, H., & Fitzsimmons, J. N. (2016). Hawaiian imprint on dissolved Nd and Ra isotopes and rare earth elements in the central North Pacific: Local survey and seasonal variability. *Geochimica et Cosmochimica Acta*, *189* (2016), 110–131. https://doi.org/10.1016/j.gca.2016.06.001

Geibert, W., Rodellas, V., Annett, A., Van Beek, P., Garcia-Orellana, J., Hsieh, Y., & Masque, P. (2013). 226Ra determination via the rate of ^{222}Rn ingrowth with the radium delayed coincidence counter (RaDeCC). *Limnology and Oceanography: Methods*, *11*, 594–603. https://doi.org/10.4319/lom.2013.11.594

Gordon, R. M., Coale, K. H., & Johnson, K. S. (1997). Iron distributions in the equatorial Pacific: Implications for new production. *Limnology & Oceanography*, *42*(3), 419–431. https://doi.org/10.4319/lo.1997.42.3.0419

Hammond, D. E., Marton, R. A., Berelson, W. M., & Ku, T. L. (1990). Radium 228 distribution and mixing in San Nicolas and San Pedro basins, southern California borderland. *Journal of Geophysical Research*, *95*(C3), 3321–3335. https://doi.org/10.1029/JC095iC03p03321

Hautala, S. L. (2018). The abyssal and deep circulation of the Northeast Pacific Basin. *Progress in Oceanography*, *160*, 68–82. https://doi.org/10.1016/j.pocean.2017.11.011

Hautala, S. L., & Roemmich, D. H. (1998). Subtropical mode water in the northeast Pacific basin. *Journal of Geophysical Research*, *103*(C6), 13055–13066. https://doi.org/10.1029/98jc01015

Henderson, P. B., Morris, P. J., Moore, W. S., & Charette, M. A. (2013). Methodological advances for measuring low-level radium isotopes in seawater. *Journal of Radioanalytical and Nuclear Chemistry*, *296*(1), 357–362. https://doi.org/10.1007/s10967-012-2047-9

Hult, M., Charette, M., Lutter, G., Marissens, G., Henderson, P., Sobiech-Matura, K., & Simgen, H. (2019). Underground gamma-ray measurements of radium isotopes from hydrothermal plumes in the deep Pacific Ocean. *Applied Radiation and Isotopes*, *153*, 108831. https://doi.org/10.1016/j.apradiso.2019.108831

Hult, M., Lutter, G., Marissens, G., & Stroh, H. (2020). *Serving policy and science at the HADES underground research facility - a casebook*. EUR 30207 EN, Publications Office of the European Union. https://doi.org/10.2760/056079,JRC120311

Kadko, D., Cochran, J. K., & Lyle, M. (1987). The effect of bioturbation and adsorption gradients on solid and dissolved radium profiles in sediments from the eastern equatorial Pacific. *Geochimica et Cosmochimica Acta*, *51*(6), 1613–1623. https://doi.org/10.1016/0016-7037(87)90342-5

Kaufman, A., Trier, R. M., Broecker, W. S., & Feely, H. W. (1973). Distribution of ^{228}Ra in the world ocean. *Journal of Geophysical Research*, *78*(36), 8827–8848. https://doi.org/10.1029/JC078i036p08827

Kemnitz, N., Hammond, D. E., Henderson, P., Le Roy, E., Charette, M. A., Moore, W. S., et al. (2022). Actinium and radium fluxes from the seabed in the northeast Pacific Basin. *Marine Chemistry*, *250*, 104180. https://doi.org/10.1016/j.marchem.2022.104180

Kemnitz, N. J. (2023). *Modeling deep ocean water and sediment dynamics in the eastern Pacific Ocean using actinium-227 and other naturally occurring radioisotopes*, Ph.D. Thesis, University of Southern California, (pp. 237)

Key, R. M., Moore, W. S., & Sarmiento, J. L. (1992a). *Transient tracers in the ocean north Atlantic study final data report for ^{228}Ra and ^{226}Ra*. Ocean Tracer Laboratory, Department of Geology and Geophysics, Princeton University, Technical Report #92-2.

Key, R. M., Moore, W. S., & Sarmiento, J. L. (1992b). *Transient tracers in the ocean tropical Atlantic study final data report for ^{228}Ra and ^{226}Ra*. Ocean Tracer Laboratory, Department of Geology and Geophysics, Princeton Univ., Technical Report #92-3.

Key, R. M., Rotter, R. J., McDonald, G. J., & Slater, R. D. (1990). Western boundary exchange experiment final data report for large volume samples ^{228}Ra, ^{226}Ra, ^{9}Be, and ^{10}Be Results. In *Technical report# 90–1, ocean tracer laboratory*. Dept. Geology and Geophysics, Princeton Univ.

Kipp, L., Charette, M., Hammond, D., & Moore, W. S. (2015). Hydrothermal vents: A previously unrecognized source of actinium-227 to the deep ocean. *Marine Chemistry*, *177*, 583–590. https://doi.org/10.1016/j.marchem.2015.09.002

Kipp, L. E., Charette, M. A., Moore, W. S., Henderson, P. B., & Rigor, I. G. (2018). Increased fluxes of shelf-derived materials to the central Arctic Ocean. *Science Advances*, *4*(1), eaao1302. https://doi.org/10.1126/sciadv.aao1302

Kipp, L. E., Kadko, D. C., Pickart, R. S., Henderson, P. B., Moore, W. S., & Charette, M. A. (2019). Shelf-Basin interactions and water mass residence times in the western Arctic Ocean: Insights provided by radium isotopes. *Journal of Geophysical Research: Oceans*. https://doi.org/10.1029/2019JC014988

Kipp, L. E., Sanial, V., Henderson, P. B., van Beek, P., Reyss, J. L., Hammond, D. E., et al. (2018b). Radium isotopes as tracers of hydrothermal inputs and neutrally buoyant plume dynamics in the deep ocean. *Marine Chemistry*, *201*, 51–65. https://doi.org/10.1016/j.marchem.2017.06.011

Koczy, F. F., Picciotto, E., Poulaert, G., & Wilgain, S. (1957). Mesure des isotopes du thorium dans l'eau de mer. *Geochimica et Cosmochimica Acta*, *11*(1–2), 103–129. https://doi.org/10.1016/0016-7037(57)90008-x

Ku, T., & Luo, S. (1994). New appraisal of radium 226 as a large-scale oceanic mixing tracer. *Journal of Geophysical Research*, *99*(C5), 10255–10273. https://doi.org/10.1029/94jc00089

Ku, T.-L., & Luo, S. (2008). Ocean circulation/mixing studies with decay-series isotopes. In S. Krishnaswami, & J. K. Cochran (Eds.), *U-Th series nuclides in aquatic systems*, (pp. 307–344). Elsevier. https://doi.org/10.1016/s1569-4860(07)00009-5

Ku, T.-L., Luo, S., Kusakabe, M., & Bishop, J. K. B. (1995). 228Ra-derived nutrient budgets in the upper equatorial Pacific and the role of "new" silicate in limiting productivity. *Deep-Sea Research*, *42*(2–3), 479–497. https://doi.org/10.1016/0967-0645(95)00020-q

Kumamoto, Y., Aoyama, M., Hamajima, Y., Aono, T., Kouketsu, S., Murata, A., & Kawano, T. (2014). Southward spreading of the Fukushima-derived radiocesium across the Kuroshio extension in the North Pacific. *Science Reports*, *4*(1), 4276. https://doi.org/10.1038/srep04276

Kwon, E. Y., Kim, G., Primeau, F., Moore, W. S., Cho, H. M., Devries, T., et al. (2014). Global estimate of submarine groundwater discharge based on an observationally constrained radium isotope model. *Geophysical Research Letters*, *41*(23), 8438–8444. https://doi.org/10.1002/2014GL061574

Lanning, N. J., Jiang, S., Amaral, V. J., Fitzsimmons, J. N., Steffen, J. M., Lam, P. J., et al. (2023). Isotopes illustrate vertical transport of anthropogenic Pb by reversible scavenging within Pacific Ocean particle veil. *Proceedings of the National Academy of Sciences*, *120*(23), e2219688120. https://doi.org/10.1073/pnas.2219688120

Le Roy, E., Charette, M. A., Henderson, P. B., Shiller, A., Moore, W. S., Kemnitz, N., et al. (2021). Controls on barium and radium-226 distributions along GEOTRACES GP15. *Goldschmidt Meeting*. https://doi.org/10.7185/gold2021.5843

Li, Y. H., Feely, H. W., & Toggweiler, J. R. (1980). ^{228}Ra and ^{228}Th concentrations in GEOSECS Atlantic surface waters. *Deep-Sea Research*, *27*(7), 545–555. https://doi.org/10.1016/0198-0149(80)90039-4

Middelburg, J. J., Soetaert, K., & Herman, P. M. (1997). Empirical relationships for use in global diagenetic models. *Deep-Sea Research*, *44*(2), 327–344. https://doi.org/10.1016/S0967-0637(96)00101-X

Moore, W. S. (1969). Measurement of Ra228 and Th228 in sea water. *Journal of Geophysical Research*, *74*(2), 694–704. https://doi.org/10.1029/jb074i002p00694

Moore, W. S. (1976). Sampling ^{228}Ra in the deep ocean. *Deep-Sea Research*, *23*(7), 647–651. https://doi.org/10.1016/0011-7471(76)90007-3

Moore, W. S. (2008). Fifteen years experience in measuring ^{224}Ra and ^{223}Ra by delayed-coincidence counting. *Marine Chemistry*, *109*(3–4), 188–197. https://doi.org/10.1016/j.marchem.2007.06.015

Moore, W. S. (2010). The effect of submarine groundwater discharge on the ocean. *Annual Review of Marine Science*, *2*(1), 59–88. https://doi.org/10.1146/annurev-marine-120308-081019

Moore, W. S., & Arnold, R. (1996). Measurement of 223Ra and 224Ra in coastal waters using a delayed coincidence counter. *Journal of Geophysical Research*, *101*(C1), 1321–1329. https://doi.org/10.1029/95jc03139

Moore, W. S., & Reid, D. F. (1973). Extraction of radium from natural waters using manganese-impregnated acrylic fibers. *Journal of Geophysical Research*, *78*(36), 8880–8886. https://doi.org/10.1029/jc078i036p08880

Moore, W. S., & Santschi, P. H. (1986). Ra-228 in the deep Indian Ocean. *Deep-Sea Research*, *33*(1), 107–120. https://doi.org/10.1016/0198-0149(86)90110-x

Moore, W. S., Sarmiento, J. L., & Key, R. M. (2008). Submarine groundwater discharge revealed by ^{228}Ra distribution in the upper Atlantic Ocean. *Nature Geoscience*, *1*(5), 309–311. https://doi.org/10.1038/ngeo183

Moore, W. S., Ussler, W., & Paull, C. K. (2008). Short-lived radium isotopes in the Hawaiian margin: Evidence for large fluid fluxes through the Puna Ridge. *Marine Chemistry*, *109*(3–4), 421–430. https://doi.org/10.1016/j.marchem.2007.09.010

Neuholz, R., Schnetger, B., Kleint, C., Koschinsky, A., Lettmann, K., Sander, S., et al. (2020). Near-field hydrothermal plume dynamics at brothers volcano (Kermadec Arc): A short-lived radium isotope study. *Chemical Geology*, *533*(16), 119379. https://doi.org/10.1016/j.chemgeo.2019.119379

Nozaki, Y., Dobashi, F., Kato, Y., & Yamamoto, Y. (1998). Distribution of Ra isotopes and the ^{210}Pb and ^{210}Po balance in surface seawaters of the mid Northern Hemisphere. *Deep-Sea Research*, *45*(8), 1263–1284. https://doi.org/10.1016/s0967-0637(98)00016-8

Rutgers van der Loeff, M. M., Key, R. M., Scholten, J., Bauch, D., & Michel, A. (1995). ^{228}Ra as a tracer for shelf water in the arctic ocean. *Deep-Sea Research*, *42*(6), 1533–1553. https://doi.org/10.1016/0967-0645(95)00053-4

Rypina, I. I., Jayne, S. R., Yoshida, S., Macdonald, A. M., & Buesseler, K. (2014). Drifter-based estimate of the 5 year dispersal of Fukushima-derived radionuclides. *Journal of Geophysical Research: Oceans*, *119*(11), 8177–8193. https://doi.org/10.1002/2014jc010306

Sanial, V., Kipp, L. E., Henderson, P. B., van Beek, P., Reyss, J. L., Hammond, D. E., et al. (2018). Radium-228 as a tracer of dissolved trace element inputs from the Peruvian continental margin. *Marine Chemistry*, *201*, 20–34. https://doi.org/10.1016/j.marchem.2017.05.008

Sarmiento, J. L., Rooth, C. G. H., & Broecker, W. S. (1982). Radium 228 as a tracer of basin wide processes in the abyssal ocean. *Journal of Geophysical Research*, *87*(C12), 9694–9698. https://doi.org/10.1029/JC087iC12p09694

SCOR. (2007). GEOTRACES–An international study of the global marine biogeochemical cycles of trace elements and their isotopes. *Geochemistry*, *67*, 85–131.

Slemons, L., Paul, B., Resing, J., & Murray, J. W. (2012). Particulate iron, aluminum, and manganese in the Pacific equatorial undercurrent and low latitude western boundary current sources. *Marine Chemistry*, *142*, 54–67. https://doi.org/10.1016/j.marchem.2012.08.003

Soda (2023). data from http://apdrc.soest.hawaii.edu/datadoc/soda_3.3.1.php

Stabeno, P. J., Reed, R. K., & Schumacher, J. D. (1995). The Alaska coastal current: Continuity of transport and forcing. *Journal of Geophysical Research*, *100*(C2), 2477–2485. https://doi.org/10.1029/94jc02842

Tazoe, H., Obata, H., Hara, T., Inoue, M., Tanaka, T., & Nishioka, J. (2022). Vertical profiles of ^{226}Ra and ^{228}Ra activity concentrations in the western subarctic gyre of the Pacific Ocean. *Frontiers in Marine Science*, *9*. https://doi.org/10.3389/fmars.2022.824862

Vieira, L. H., Achterberg, E. P., Scholten, J., Beck, A. J., Liebetrau, V., Mills, M. M., & Arrigo, K. R. (2019). Benthic fluxes of trace metals in the Chukchi Sea and their transport into the Arctic Ocean. *Marine Chemistry*, *208*, 43–55. https://doi.org/10.1016/j.marchem.2018.11.001

Yamada, M., & Nozaki, Y. (1986). Radium isotopes in coastal and open ocean surface waters of the Western North Pacific. *Marine Chemistry*, *19*(4), 379–389. https://doi.org/10.1016/0304-4203(86)90057-5

You, Y. (2003). The pathway and circulation of North Pacific intermediate water. *Geophysical Research Letters*, *30*, 24–27. https://doi.org/10.1029/2003GL018561

Zhou, H., Liu, H., Tan, S., Yang, W., Li, Y., Liu, X., et al. (2021). The observed North Equatorial countercurrent in the far western Pacific Ocean during the 2014–16 El Niño. *Journal of Physical Oceanography*, *51*, 2003–2020. https://doi.org/10.1175/jpo-d-20-0293.1